Magma Storage System and Hidden Hotspot Track of the Emeishan Large Igneous Province and its Impact on the Timing of the Capitanian Mass Extinction

Yiduo Liu[1, 6], Lun Li[2, 3, 6], Jolante van Wijk[4], Aibing Li[1], Yuanyuan V. Fu[5]

[1] *Department of Earth and Atmospheric Sciences, University of Houston, Houston, Texas 77204, USA*

[2] *Guangdong Provincial Key Lab of Geodynamics and Geohazards, School of Earth Sciences and Engineering, Sun Yat-sen University, Guangzhou, Guangdong 510275, China*

[3] *Southern Marine Science and Engineering Guangdong Laboratory (Zhuhai), Zhuhai, Guangdong 510999, China*

[4] *Department of Earth and Environmental Science, New Mexico Institute of Mining and Technology, Socorro, New Mexico 87801, USA*

[5] *Key Laboratory of Earthquake Prediction, Institute of Earthquake Forecasting, China Earthquake Administration, Beijing, 100036, China*

[6] *These authors contributed equally. Correspondence to: Lun Li (lilun6@mail.sysu.edu.cn).*

ABSTRACT

Large igneous provinces (LIPs) are often associated with mass extinctions and are vital for life evolution on Earth. However, the precise relation between LIPs and their impacts on biodiversity is enigmatic as they can be asynchronous. If the environmental impacts are primarily

related to sill emplacement, the structure of LIPs' magma storage system becomes critical as it dictates the occurrence and timing of mass extinction. Here we use surface wave tomography to image the lithosphere under the Permian Emeishan Large Igneous Province (ELIP) in SW China. We find a NE-trending zone of high shear-wave velocity (Vs) and negative radial anisotropy (Vsv > Vsh) in the crust and lithosphere and interpret it as a mafic-ultramafic, dike-dominated magma storage system on the hidden hotspot track of the ELIP. An area of less-negative radial anisotropy, on the hotspot track but away from the eruption center, reflects an elevated proportion of sills emplaced at the incipient stage of the ELIP. Liberation of poisonous gases and mercury by the sills explains why the mid-Capitanian global biota crisis preceded the peak ELIP eruption by 2-3 million years.

INTRODUCTION

Large igneous provinces are characterized by rapid emplacement of predominantly mafic magma in the lithosphere and volcanic eruptions forming plateau basalts in an area greater than 10^5 km^2 (Bryan and Ernst, 2008). Many LIPs have been associated with abrupt environmental catastrophes and mass extinction events (Sobolev et al., 2011; Ernst, 2014). While several LIP-related extinctions occurred during or shortly after the major volcanic phase of the corresponding LIPs (Bond and Wignall, 2014), some preceded the major phase, leaving an enigma on the exact temporal relationship between LIPs and the associated mass extinctions.

The structure of magma storage systems of LIPs, particularly sill emplacement, is a key to understanding this relation (Svensen et al., 2009). Modern hotspots, such as Yellowstone, display the magma storage system of actively forming LIPs (Jiang et al., 2018). However, they do not provide direct constraint on the timing of mass extinction. Ancient LIPs, by contrast,

potentially preserve a complete picture of magma storage systems and thus offer an opportunity to document their structures and assess the environmental consequences.

Here we study the seismic structure of the Emeishan Large Igneous Province (ELIP) in SW China based on a new surface wave tomography model. The ELIP is so far the only candidate that caused a global biota crisis in the mid-Capitanian (~262 Ma) (Wignall et al., 2009; Bond et al., 2019), which preceded the major volcanic activity (260-257 Ma) (Shellnutt et al., 2012). We attempt to characterize the ELIP's magma storage system and address the unusual asynchrony.

GEOLOGICAL BACKGROUND

The ELIP is located in the western Yangtze craton of the South China block (Fig.1A-B). It comprises mainly tholeiitic continental flood basalts, with a lesser amount of picrites, lamproites, gabbros, pyroxenites, and others (e.g., Chung and Jahn, 1995; Xu et al., 2004). These rocks were mainly derived from the sub-lithospheric mantle and emplaced in the South China block (Chung and Jahn, 1995; He et al., 2003; Xu et al., 2004; Zhou et al., 2005). The southwestern corner of ELIP is offset left-laterally by the Cenozoic Ailao Shan-Red River shear zone and poorly exposed. The larger, better preserved northeastern part, covering at least ~2.5-3 $\times 10^5$ km^2, is divided into three concentric zones (inner, intermediate, and outer) that represent a decrease in flood basalt thickness outward (He et al., 2003; Xu et al., 2004). Before the ELIP eruption, the Maokou Formation that deposited on the Yangtze carbonate platform underwent erosion and karstification (He et al., 2003; Xiao et al., 2016), resulting in varying remnant thickness. In particular, a NE-trending belt of anomalously thin thickness extends from the uplift center to the Sichuan Basin (Fig.1C and Supplementary File).

Paleomagnetic studies show an equatorial paleo-latitude for the ELIP at the time of eruption and an overall clockwise rotation of ~27° since 260 Ma (Huang et al., 2018). Magmatic underplating occurred at the Moho depth, as evidenced by high density, high seismic wave velocity, high Vp/Vs ratios, and thickened crust (Chen et al., 2015). A pronounced positive residual gravity anomaly spreads from the ELIP center to the Sichuan Basin and is attributed to ELIP intrusions (Deng et al., 2014).

SURFACE WAVE TOMOGRAPHY: METHODS AND RESULTS

We developed a radially anisotropic shear wave velocity model of the lithosphere under the ELIP region from Rayleigh wave and Love wave phase velocity at periods of 8-167 s. Rayleigh and Love waves are primarily sensitive to vertically (Vsv) and horizontally (Vsh) polarized shear-wave velocities, respectively. Radial anisotropy, defined as 100%*(Vsh-Vsv)/Vs where Vs is the Voigt average of Vsh and Vsv, exploits the variations between the two waves by assuming hexagonal anisotropy with a vertical symmetry axis (Babuska and Cara, 1991). Radial anisotropy may be induced by lattice preferred orientation of minerals such as mica, olivine, and pyroxene (Shapiro et al., 2004; Silver and Chan, 1991), or by shape preferred orientation of macro-scale structures such as fractures, foliation, and magma (Silver and Chan, 1988; Emmermann and Lauterjung, 1997).

Our shear wave velocity model (Figs. 2-3 & S12-S14) shows a high velocity at 15-220 km depths beneath the Yangtze craton east of the Xianshuihe-Xiaojiang fault, and a low velocity zone in the crust of the southeastern Tibetan Plateau. These results agree with previous studies: high velocity anomaly dominates the Yangtze craton at 15-240 km depths due to the cold and

91 thick cratonic lithosphere, while the low velocity zone is related to the thickened, partially-
92 molten mid- to lower crust in Tibet (Huang et al., 2010).
93 Radial anisotropy results show profound lateral and vertical variations in the crust and
94 upper lithospheric mantle (Figs. 2-3 & S15). Positive radial anisotropy (Vsh > Vsv) is found in
95 the middle and lower crust (15 km - Moho) under the SE Tibetan Plateau, which is interpreted as
96 the sub-horizontal alignment of mica due to ductile deformation induced by the India-Asia
97 collision (Shapiro et al., 2004). Another zone of positive radial anisotropy is located around the
98 southern Xianshuihe-Xiaojiang fault. This region is also associated with low shear wave
99 velocities (Figs. 2-3 & S14-S15). We explain this as sub-horizontal ductile deformation in the
100 middle and lower crust due to the lateral expansion of the Tibetan Plateau (Copley, 2008). In the
101 lithospheric mantle below 80 km, positive radial anisotropy is present ubiquitously; similar
102 positive radial anisotropy patterns have been described from other cratons (Nettles and
103 Dziewoński, 2008). This largely results from the lattice preferred orientation of olivine in
104 horizontal planes.
105 The most intriguing phenomenon is a NE-trending coherent zone of negative radial
106 anisotropy (Vsv > Vsh) associated with a high velocity anomaly that underlies the inner and
107 intermediate zones of the ELIP (Figs. 2 & 3). It shows as a broad zone in the shallow crust (0-15
108 km) and can be traced downward to ~80 km depth. Such a zone of reduced radial anisotropy is
109 still detectable down to 120 km depth within the Yangtze craton (Figs. 2 & S15). The amplitude
110 of the negative radial anisotropy is mostly around -2% but is as strong as -4% in the lower crust
111 under the Sichuan Basin. A similar body of negative radial anisotropy was imaged, but not
112 interpreted, at 20-35 km depths by Huang et al. (2010). Another study (Xie et al., 2013) found a
113 narrow zone of negative anisotropy in the middle and upper crust under eastern Tibet and

ascribed it to faults and cracks. However, the presence of faults and cracks cannot explain the observed combination of high velocity and negative radial anisotropy that extends into the mantle lithosphere under the Sichuan Basin.

DISCUSSION

Geological Interpretation on the High Velocity, Negative Radial Anisotropy Zone

Negative radial anisotropy in the crust and upper mantle is often explained by the sub-vertical alignment of mineral crystals such as mica and olivine, macroscopic structures such as faults and shear zones, or partial melts (Shapiro et al., 2004; Xie et al., 2013). One explanation for our case could be lithospheric-scale faulting or partial melting from the Tibetan Plateau. Although it cannot be ruled out, this interpretation is not realistic because (1) the NE-trending negative radial anisotropy zone is not parallel to the N-trending Xiaojiang fault, nor the NW-trending Ailao Shan-Red River shear zone, (2) lithospheric-scale, high-strain structures *within* the craton that could form vertical alignment are not observed, and (3) such interpretations would produce low, rather than high, shear-wave velocities.

Noticing the southern end of the negative radial anisotropy body coincides with the eruption- and domal uplift centers of the ELIP, we propose an alternative interpretation that connects the seismic signature with the shape preferred orientation of magma systems (Fig. 4A). A magma storage system of a LIP consists of a network of dikes, sills, laccoliths, and magma chambers, by which magma is transported through and stored within the lithosphere (Ernst et al., 2019). The geometry of such a system can be simplified into two end-members in the scope of seismic radial anisotropy: vertical dikes, and horizontal sills. The thickness of a single dike or sill

136 is usually below the detection limit of seismic waves; in groups, however, they can be
137 seismically detectable (Backus, 1962).
138 For a transversely isotropic media of mafic to felsic compositions with a vertical or
139 horizontal symmetry (Eshelby, 1957), the presence of dikes and sills of mafic-ultramafic
140 compositions (i.e., higher Mg and Fe contents) can effectively alter the bulk elastic properties of
141 the medium (Fig. 4A). The bulk Vs and radial anisotropy of a medium with a dike-dominated
142 system both decrease at the time of intrusion; after the magma solidifies and cools, Vs increases
143 while the radial anisotropy remains depleted. For a sill-dominated system, Vs decreases first, and
144 increases after cooling, while the radial anisotropy remains elevated.
145 The observed body of negative radial anisotropy and high Vs (anomalies "a" and "c",
146 Fig. 3) can thus be interpreted as the solidified magma storage system of the ELIP that is
147 dominated by sub-seismic-scale, densely-spaced, mafic-ultramafic dikes. Field observations of
148 the ELIP dike swarm system (Li et al., 2015) support this interpretation. Anomaly "b" (Fig. 3),
149 characterized by thicker crust, higher Vs, and less-negative radial anisotropy than "a" and "c",
150 cannot be explained by a reduction of intrusions; instead, it reflects a greater amount of intrusion
151 with a higher fraction of sills.
152 One may suggest that alternatively, the paired anomaly of negative radial anisotropy and
153 high Vs may be attributed to the Neoproterozoic rifting and magmatism in South China during
154 the Rodinia breakup (Li et al., 1999). While it equally explains all the geophysical results, it
155 leaves the Permian volcanism and the erosion of Maokou Formation in the Sichuan Basin
156 unexplained (Fig. 1). Thus, we favor the Permian ELIP interpretation.
157
158 **Tectonic and Environmental Implications**

Tectonic reconstruction lends further support to our interpretation (Fig. 4B). Paleomagnetic studies show that the South China block was moving northward around 260 Ma and it has experienced an overall ~27° clockwise rotation since then (Huang et al., 2018). If the Emeishan hotspot was stationary, the predicted hotspot track should align N-S in Permian, i.e., NE-SW at present. The zone of reduced radial anisotropy and high Vs at 15-120 km depths trends NE through the eruption center (Fig. 2 & S15) and overlaps the positive residual gravity anomaly (Deng et al., 2014). Therefore, this 700-km long anomaly represents the Emeishan hotspot track that is concealed in the Yangtze craton.

Lithospheric thickness variations affect the route of magma transport and storage and the location of eruption. A schematic section A-A" illustrates how the magma system developed through time (Figs. 4C-D). In the mid- to late Guadalupian (middle Permian), a mantle upflow reached the base of the thick craton and generated melt at the base of lithosphere. Its surface responses include gentle uplift, erosion, and karstification of the middle-Permian Maokou carbonate rocks in the Sichuan Basin; only little magma succeeded to penetrate the lithosphere (Fig. 1B). As the South China block drifted northward, more melt formed and infiltrated the craton, mainly as dikes. Melt at the base of the lithosphere did not find an "easy way" out until the thinner margin of the Yangtze craton was above the mantle upflow. In the upper crust, the Xiaojiang normal fault and the Panxi rift were (re-)activated before and during the onset of the ELIP (He et al., 2003; Li et al., 2015), facilitated the erosion of Maokou Formation and the magmatic emplacement.

Approaching the ELIP inner zone from the northeast, the radial anisotropy at "b" is not as depleted as "c" under the Sichuan Basin at 15 km – Moho depth (Figs. 2 & 3), but its Vs is higher. This suggests a higher fraction of sills, consistent with the magma underplating locally

(Chen et al., 2015) and volcanic systems in general (Jaxybulatov et al., 2014). Emplacement of laterally extensive sills tends to take place in mechanical layers (Kavanagh et al., 2006) such as sedimentary basins in the uppermost crust, near the brittle-ductile transition, and crust-mantle interface. Sills efficiently store magma over large areas, and liberate large volumes of greenhouse gases and mercury that may trigger catastrophic environmental change (Svensen et al., 2009). Indeed, above "b", the 263-Ma Panzhihua layered mafic intrusions intruded and metamorphosed the Dengying dolomitic limestones in the shallow crust (Zhou et al., 2005), which triggered the degassing and release of mercury that caused the mid-Capitanian mass extinction.

As the South China block kept moving northward and the major eruption occurred, the release of volatiles and mercury also continued to the Guadalupian-Lopingian boundary (260 Ma) (Huang et al., 2019). After the magma crystallized, the ELIP strengthened the Yangtze craton and controlled the geometry of the Himalayan-Tibetan orogen (Xu et al., 2020).

This study highlights how surface wave tomography can be used to characterize the architecture of the magma storage system of LIPs and explain the relation among hotspot volcanism, lithosphere, and biosphere. Similar studies can be conducted for other LIPs, which may enable future models to evaluate the environment impacts in a more quantitative way.

ACKNOWLEDGMENTS

Seismic data were collected by participants of the MIT-CIGMR seismic network and archived at the IRIS Data Management Center. LL acknowledges the funds from NSFC (No. 41804043, 41874102) and the Second Tibetan Plateau Scientific Expedition and Research Program (STEP)

(No. 2019QZKK0701). YL acknowledges the GURI Fund from the State of Texas and University of Houston.

REFERENCES CITED

Babuska, V., and Cara, M., 1991, Seismic anisotropy in the Earth: Kluwer, Dordrecht, Netherlands, Modern Approaches in Geophysics, v. 10, 219 p.

Backus, G.E., 1962, Long-wave elastic anisotropy produced by horizontal layering: Journal of Geophysical Research: Solid Earth, v. 67, p. 4427-4440, https://doi.org/10.1029/JZ067i011p04427

Bond, D.P., and Wignall, P.B., 2014, Large igneous provinces and mass extinctions: an update, in Keller, G., and Kerr, A.C., eds, Volcanism, Impacts, and Mass Extinctions: Causes and Effects: Geological Society of America Special Papers 505, p. 29-55.

Bond, D.P., Wignall, P.B., and Grasby, S.E., 2019, The Capitanian (Guadalupian, Middle Permian) mass extinction in NW Pangea (Borup Fiord, Arctic Canada): A global crisis driven by volcanism and anoxia: Geological Society of America Bulletin, B35281.1, https://doi.org/10.1130/B35281.1.

Bryan, S.E., and Ernst, R.E., 2008, Revised definition of large igneous provinces (LIPs): Earth-Science Reviews, v. 86(1-4), p. 175-202, https://doi.org/10.1016/j.earscirev.2007.08.008.

Chen, Y., Xu, Y., Xu, T., Si, S., Liang, X., Tian, X., Deng, Y., Chen, L., Wang, P., Xu, Y., and Lan, H., 2015, Magmatic underplating and crustal growth in the Emeishan Large Igneous Province, SW China, revealed by a passive seismic experiment: Earth and Planetary Science Letters, v. 432, p. 103-114, https://doi.org/10.1016/j.epsl.2015.09.048.

Chung, S.L., and Jahn, B.M., 1995, Plume-lithosphere interaction in generation of the Emeishan

flood basalts at the Permian-Triassic boundary: Geology, v. 23(10), p. 889-892, https://doi.org/10.1130/0091-7613(1995)023<0889:PLIIGO>2.3.CO;2.

Copley, A., 2008, Kinematics and dynamics of the southeastern margin of the Tibetan Plateau: Geophysical Journal International, v. 174(3), p. 1081-1100, https://doi.org/10.1111/j.1365-246X.2008.03853.x.

Deng, Y., Zhang, Z., Mooney, W., Badal, J., Fan, W., and Zhong, Q., 2014, Mantle origin of the Emeishan large igneous province (South China) from the analysis of residual gravity anomalies: Lithos, v. 204, p. 4-13. https://doi.org/10.1016/j.lithos.2014.02.008

Emmermann, R., and Lauterjung, J., 1997, The German continental deep drilling program KTB: overview and major results: Journal of Geophysical Research: Solid Earth, v. 102(B8), p. 18179-18201, https://doi.org/10.1029/96JB03945.

Ernst, R.E., 2014, Large Igneous Provinces: Cambridge University Press, 653 p.

Ernst, R.E., Liikane, D.A., Jowitt, S.M., Buchan, K.L., and Blanchard, J.A., 2019, A new plumbing system framework for mantle plume-related continental Large Igneous Provinces and their mafic-ultramafic intrusions: Journal of Volcanology and Geothermal Research, v. 384, p. 75-84. https://doi.org/10.1016/j.jvolgeores.2019.07.007.

Eshelby, J.D., 1957. The determination of the elastic field of an ellipsoidal inclusion, and related problems. Proceedings of the Royal Society of London, ser. A, v. 241(1226), p. 376-396, https://doi.org/10.1098/rspa.1957.0133.

He, B., Xu, Y.G., Chung, S.L., Xiao, L., and Wang, Y., 2003, Sedimentary evidence for a rapid, kilometer-scale crustal doming prior to the eruption of the Emeishan flood basalts: Earth and Planetary Science Letters, v. 213(3-4), p. 391-405, https://doi.org/10.1016/S0012-821X(03)00323-6.

Huang, B., Yan, Y., Piper, J.D., Zhang, D., Yi, Z., Yu, S., and Zhou, T., 2018, Paleomagnetic constraints on the paleogeography of the East Asian blocks during Late Paleozoic and Early Mesozoic times: Earth-Science Reviews, v. 186, p. 8-36, https://doi.org/10.1016/j.earscirev.2018.02.004.

Huang, H., Yao, H., and van der Hilst, R.D., 2010, Radial anisotropy in the crust of SE Tibet and SW China from ambient noise interferometry: Geophysical Research Letters, v. 37(21), L21310, https://doi.org/10.1029/2010GL044981

Huang, Y., Chen, Z.Q., Wignall, P.B., Grasby, S.E., Zhao, L., Wang, X., and Kaiho, K., 2019, Biotic responses to volatile volcanism and environmental stresses over the Guadalupian-Lopingian (Permian) transition: Geology, v. 47(2), p. 175-178, https://doi.org/10.1130/G45283.1.

Jaxybulatov, K., Shapiro, N.M., Koulakov, I., Mordret, A., Landès, M., and Sens-Schoenfelder, C., 2014, A large magmatic sill complex beneath the Toba caldera: Science, v. 346(6209), p. 617-619, https://doi.org/10.1126/science.1258582.

Jiang, C., Schmandt, B., Farrell, J., Lin, F.C., and Ward, K.M., 2018, Seismically anisotropic magma reservoirs underlying silicic calderas: Geology, v. 46(8), p. 727-730, https://doi.org/10.1130/G45104.1.

Kavanagh, J.L., Menand, T., and Sparks, R.S.J., 2006, An experimental investigation of sill formation and propagation in layered elastic media: Earth and Planetary Science Letters, v. 245(3-4), p. 799-813, https://doi.org/10.1016/j.epsl.2006.03.025.

Li, H., Zhang, Z., Ernst, R., Lü, L., Santosh, M., Zhang, D., and Cheng, Z., 2015, Giant radiating mafic dyke swarm of the Emeishan Large Igneous Province: Identifying the mantle plume centre: Terra Nova, v. 27(4), p. 247-257, https://doi.org/10.1111/ter.12154.

Li, Z.X., Li, X.H., Kinny, P.D., and Wang, J., 1999. The breakup of Rodinia: did it start with a mantle plume beneath South China?: Earth and Planetary Science Letters, v. 173(3), p. 171-181. https://doi.org/10.1016/S0012-821X(99)00240-X.

Nettles, M., and Dziewoński, A.M., 2008, Radially anisotropic shear velocity structure of the upper mantle globally and beneath North America: Journal of Geophysical Research: Solid Earth, v. 113(B2), B02303, https://doi.org/10.1029/2006JB004819.

Shapiro, N.M., Ritzwoller, M.H., Molnar, P., and Levin, V., 2004, Thinning and flow of Tibetan crust constrained by seismic anisotropy: Science, v. 305(5681), p. 233-236, https://doi.org/10.1126/science.1098276.

Shellnutt, J.G., Denyszyn, S.W., and Mundil, R., 2012, Precise age determination of mafic and felsic intrusive rocks from the Permian Emeishan large igneous province (SW China): Gondwana Research, v. 22(1), p. 118-126, https://doi.org/10.1016/j.gr.2011.10.009.

Silver, P.G., and Chan, W.W., 1988, Implications for continental structure and evolution from seismic anisotropy: Nature, v. 335(6185), p. 34-39, https://doi.org/10.1038/335034a0.

Silver, P.G., and Chan, W.W., 1991, Shear wave splitting and subcontinental mantle deformation: Journal of Geophysical Research: Solid Earth, v. 96(B10), p. 16429-16454, https://doi.org/10.1029/91JB00899.

Sobolev, S.V., Sobolev, A.V., Kuzmin, D.V., Krivolutskaya, N.A., Petrunin, A.G., Arndt, N.T., Radko, V.A., and Vasiliev, Y.R., 2011, Linking mantle plumes, large igneous provinces and environmental catastrophes: Nature, v. 477(7364), p. 312-316, https://doi.org/10.1038/nature10385.

Svensen, H., Planke, S., Polozov, A.G., Schmidbauer, N., Corfu, F., Podladchikov, Y.Y., and Jamtveit, B., 2009, Siberian gas venting and the end-Permian environmental crisis: Earth

and Planetary Science Letters, v. 277(3-4), p. 490-500. https://doi.org/10.1016/j.epsl.2008.11.015.

Wignall, P.B., Sun, Y., Bond, D.P., Izon, G., Newton, R.J., Védrine, S., Widdowson, M., Ali, J.R., Lai, X., Jiang, H., and Cope, H., 2009, Volcanism, mass extinction, and carbon isotope fluctuations in the Middle Permian of China: Science, v. 324(5931), p. 1179-1182, https://doi.org/10.1126/science.1171956.

Xiao, D., Tan, X., Xi, A., Liu, H., Shan, S., Xia, J., Cheng, Y., and Lian, C., 2016, An inland facies-controlled eogenetic karst of the carbonate reservoir in the Middle Permian Maokou Formation, southern Sichuan Basin, SW China: Marine and Petroleum Geology, v. 72, p. 218-233. https://doi.org/10.1016/j.marpetgeo.2016.02.001.

Xie, J., Ritzwoller, M.H., Shen, W., Yang, Y., Zheng, Y., and Zhou, L., 2013, Crustal radial anisotropy across eastern Tibet and the western Yangtze craton: Journal of Geophysical Research: Solid Earth, v. 118(8), p. 4226-4252, https://doi.org/10.1002/jgrb.50296.

Xu, X., Zuza, A.V., Yin, A., Lin, X., Chen, H., and Yang, S., 2020. Permian plume-strengthened Tarim lithosphere controls the Cenozoic deformation pattern of the Himalayan-Tibetan orogen: Geology, v. 49. https://doi.org/10.1130/G47961.1.

Xu, Y.G., He, B., Chung, S.L., Menzies, M.A., and Frey, F.A., 2004, Geologic, geochemical, and geophysical consequences of plume involvement in the Emeishan flood-basalt province: Geology, v. 32(10), p. 917-920, https://doi.org/10.1130/G20602.1.

Zhou, M.F., Robinson, P.T., Lesher, C.M., Keays, R.R., Zhang, C.J., and Malpas, J., 2005, Geochemistry, petrogenesis and metallogenesis of the Panzhihua gabbroic layered intrusion and associated Fe-Ti-V oxide deposits, Sichuan Province, SW China: Journal of Petrology, v. 46(11), p. 2253-2280, https://doi.org/10.1093/petrology/egi054.

FIGURE CAPTIONS

Figure 1. Geologic map of the Emeishan Large Igneous Province (ELIP). (A) Index map. IC, Indochina; IN, India Plate; NC, North China; SC, South China; TP, Tibetan Plateau. (B) Map of the ELIP, showing eruption center, uplift center, flood basalts exposed on surface and drilled in wells, buried volcanic craters, basaltic dikes, and borders of the inner (I),intermediate (II), and outer (III) zones. ASRRSZ, Ailao Shan-Red River Shear Zone; LMST, Longmen Shan thrust belt; XXF, Xianshuihe-Xiaojiang Fault. (C) Isopach map of the remnant Maokou Formation deposited on the Yangtze carbonate platform prior to the ELIP. Additional contours of 160 and 250 m are shown as dashed lines. See Supplementary File for data sources.

Figure 2. 3-D isotropic shear wave velocity models (Vs) (A-E) and radial anisotropy (γ) (F-J) beneath the ELIP at depths of 0-100 km. Shear wave velocity (Vs) is calculated via a Voigt average $V_S = \sqrt{(2V_{sv}^2 + V_{sh}^2)/3}$ and radial seismic anisotropy is defined as the percentage difference between Vsh and Vsv in the medium: γ = (Vsh−Vsv)/Vs. TP, Tibetan Plateau; YZC, Yangtze Craton.

Figure 3. Cross-section AA’ showing (A) topography, (B) absolute isotropic Vs, and (C) radial seismic anisotropy. Location of AA’ is shown in Fig. 2. Anomalies “a”, “b”, and “c” are discussed in the text.

Figure 4. Geologic interpretations. (A) Effects of mafic-ultramafic magma systems on seismic properties (bulk shear-wave velocity and radial anisotropy) due to different geometry and

temperature. (B) Plate reconstruction at 260 Ma (after Huang et al. 2018) with plate boundaries and velocity vectors. The South China block is highlighted in yellow. Red dashed line indicates the inferred hotspot track and the location of transect A-A" that contains our seismic image A-A'. (C) Integrated section along the Emeishan hotspot track. Dikes, sills, flood basalts, and faults are not to scale. (D) Cartoons along A-A", showing northward-drifting Yangtze craton, mantle upflow, intrusions, and surface uplift (not to scale).

[1]GSA Data Repository item 202Xxxx, Methods, notes, and supplementary figures, is available online at www.geosociety.org/pubs/ft20XX.htm, or on request from editing@geosociety.org.

Figure 1

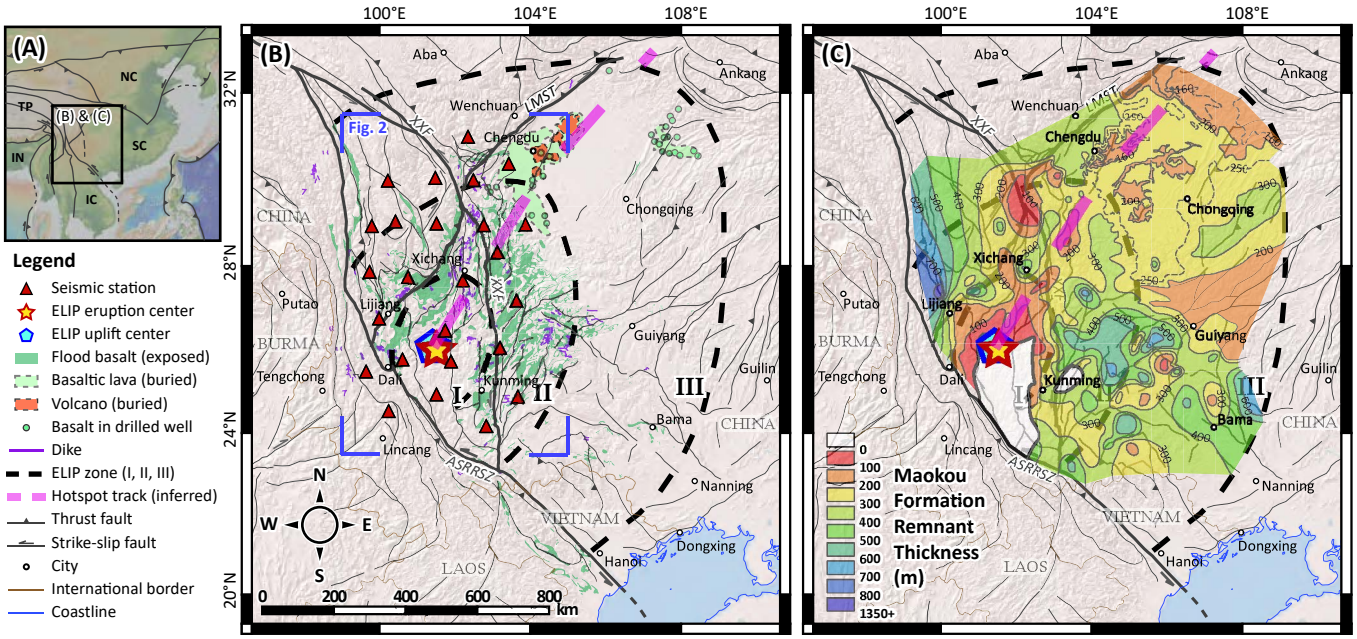
(A)
NC
TP
(B) & (C)
SC
IN
IC
Legend
Seismic station
ELIP eruption center
ELIP uplift center
Flood basalt (exposed)
Basaltic lava (buried)
Volcano (buried)
Basalt in drilled well
Dike
ELIP zone (I, II, III)
Hotspot track (inferred)
Thrust fault
Strike-slip fault
City
International border
Coastline
(B)
(C)
100°E
104°E
108°E
32°N
28°N
24°N
20°N
Aba
Ankang
Wenchuan
LMST
XXF
Chengdu
Fig. 2
Chongqing
CHINA
Xichang
Putao
Lijiang
BURMA
Guiyang
Tengchong
Dali
Kunming
Guilin
I
II
III
Bama
Lincang
ASRRSZ
Nanning
VIETNAM
Dongxing
Hanoi
LAOS
N
W
E
S
0
200
400
600
800
km
Maokou Formation Remnant Thickness (m)
0
100
200
300
400
500
600
700
800
1350+

Figure 2

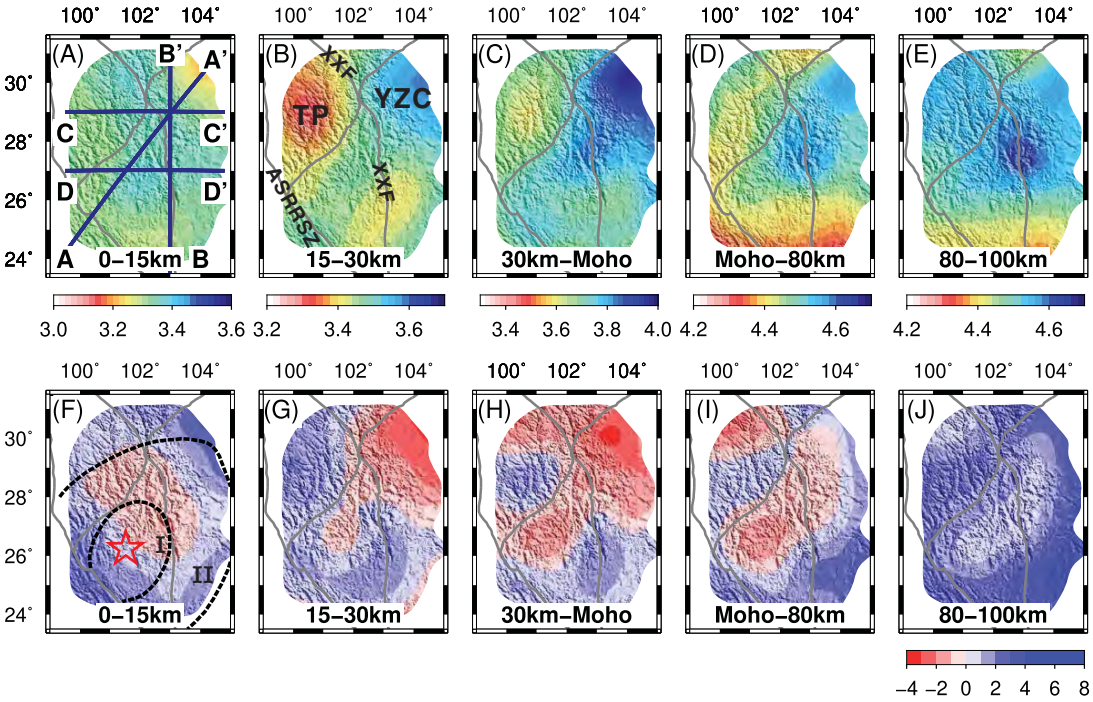
(A)
B'
A'
C
C'
D
D'
A
0–15km
B
(B)
XXF
YZC
TP
ASRRSZ
XXF
15–30km
(C)
30km–Moho
(D)
Moho–80km
(E)
80–100km
100°
102°
104°
30°
28°
26°
24°
3.0
3.2
3.4
3.6
3.2
3.4
3.6
3.4
3.6
3.8
4.0
4.2
4.4
4.6
4.2
4.4
4.6
(F)
I
II
0–15km
(G)
15–30km
(H)
30km–Moho
(I)
Moho–80km
(J)
80–100km
–4
–2
0
2
4
6
8

Figure 3

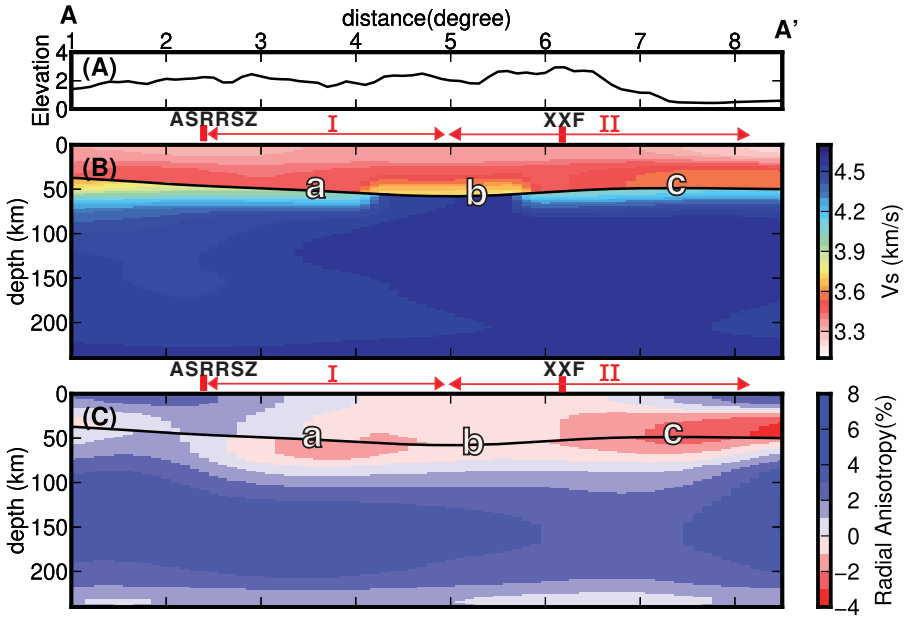
A
distance(degree)
A'
1
2
3
4
5
6
7
8
Elevation
4
2
0
(A)
ASRRSZ
I
XXF
II
(B)
depth (km)
0
50
100
150
200
a
b
c
4.5
4.2
3.9
3.6
3.3
Vs (km/s)
ASRRSZ
I
XXF
II
(C)
depth (km)
0
50
100
150
200
a
b
c
8
6
4
2
0
−2
−4
Radial Anisotropy(%)

Figure 4

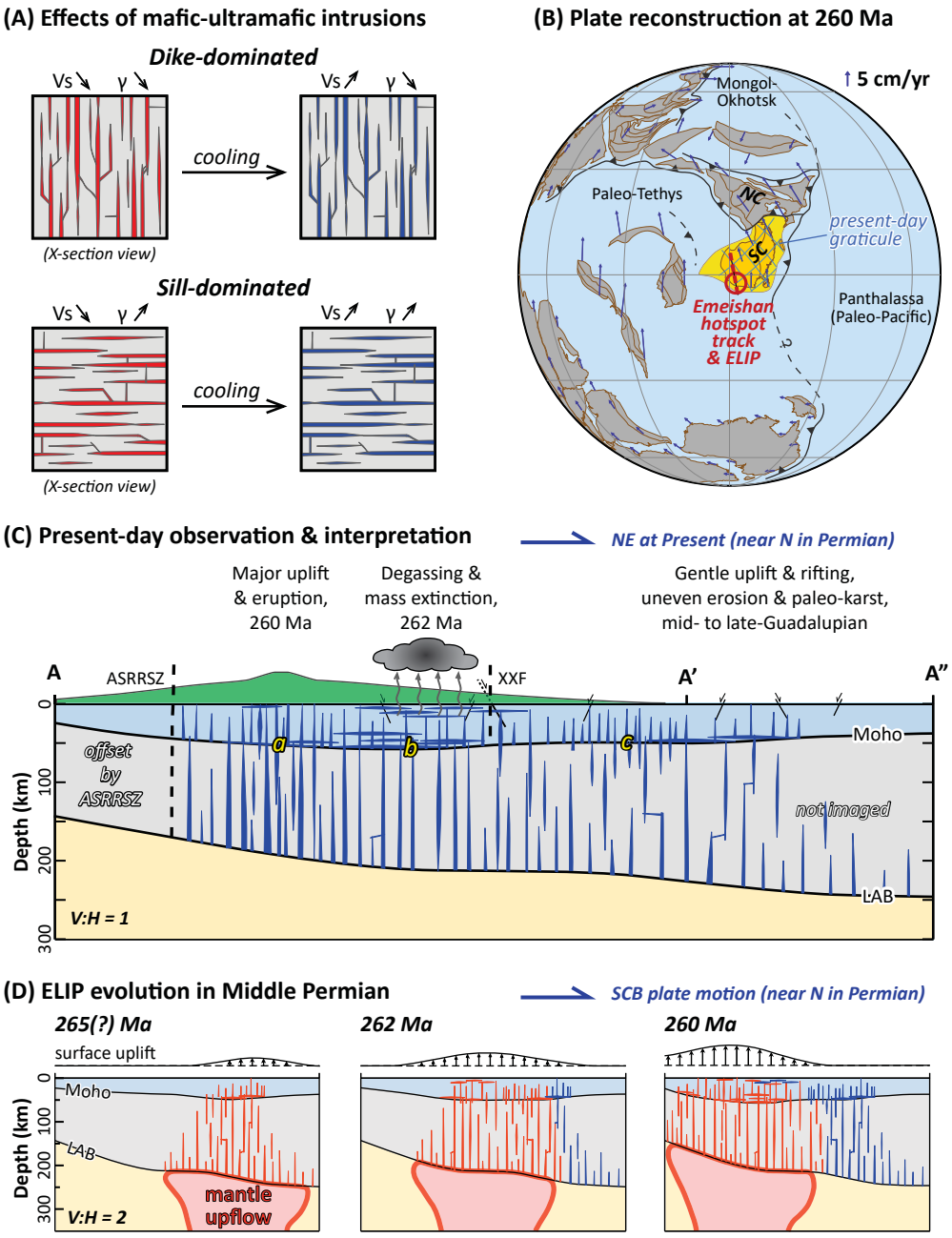
(A) Effects of mafic-ultramafic intrusions
Dike-dominated
Vs
γ
cooling
(X-section view)
Sill-dominated
(B) Plate reconstruction at 260 Ma
↑ 5 cm/yr
Mongol-Okhotsk
Paleo-Tethys
NC
SC
present-day graticule
Emeishan hotspot track & ELIP
Panthalassa (Paleo-Pacific)
(C) Present-day observation & interpretation
NE at Present (near N in Permian)
Major uplift & eruption, 260 Ma
Degassing & mass extinction, 262 Ma
Gentle uplift & rifting, uneven erosion & paleo-karst, mid- to late-Guadalupian
A
ASRRSZ
XXF
A'
A"
Moho
offset by ASRRSZ
not imaged
LAB
Depth (km)
V:H = 1
(D) ELIP evolution in Middle Permian
SCB plate motion (near N in Permian)
265(?) Ma
262 Ma
260 Ma
surface uplift
mantle upflow
V:H = 2